Bulletin of the Seismological Society of America, Vol. 95, No. 6, pp. 2462–2471, December 2005, doi: 10.1785/0120050040

A Horizontal Component Broadband Seismic Sensor Based on an Inverted Pendulum

by Elias Th. Koutsoukos and Nikolaos S. Melis

Abstract This experimental study demonstrates a horizontal seismic sensor based on an inverted vertical pendulum. The arm that keeps the proof mass inverted at the quiescent position is directly attached on an elastic metallic strip made from chrysocal ($CuSn_3Zn_9$) alloy that acts as a spring. This mass-suspension arrangement acts as pivot and restoring mechanism and reveals a relatively long natural period (3–4 sec), considering the overall dimensions of the pendulum. The application of multiple frequency-dependent feedback paths gave a flat to ground velocity response from 100 to 0.023 sec with a differential output 2×750 V/m/sec. The present study focused mainly on the pendulum arrangement with some emphasis on the suspension flexure and the feedback actuator design, whereas the electronic circuitry used was maintained according to the standard techniques used in the force-balanced sensors. Design and assembly simplicity was introduced with the use of a single uniform element as flexure without affecting the precision of the motion. Moreover, the planar coil adopted in the feedback actuator ensured a strong motor constant, without the limitations in the effective displacement usually met in the angular motion of the pendulum. Amplitude and spectral analyses of data sets obtained from local ground noise as well as from local, regional, and teleseismic earthquake activity, have been shown to be comparable with respective recordings of other standard broadband seismometers operated at the same vault. The experimental seismometer was found to be compatible with these reference seismometers in terms of amplitude and frequency response indicating the capability of the experimental sensor to resolve low-frequency and low-amplitude seismic signals.

Introduction

Many considerations regarding the linearity of motion, effective period of sensor, sensitivity, and dynamic range of passive seismic sensors have been extensively studied and speculated upon during the past years (Melton, 1979; Wielandt and Streckeisen, 1982; Riedesel *et al.*, 1990). Various alternative techniques have approached the broadening of frequency response of short-period sensors in different ways. Selective amplification of the lower part of the spectrum or direct feedback on the sensing coil has sufficiently increased the low-frequency response of seismic signals recorded by passive short-period sensors (Daniel, 1979; Willmore, 1979; Roberts, 1989). More recent approaches (Muramatsu *et al.*, 2001) involving coupled overdamped pendula techniques have shown wideband response using strong-motion non-feedback sensors.

Active sensors based on the force balance principle now dominate the field of seismic instrumentation. According to this principle, the seismic mass position is compensated or balanced by the application of an externally generated force that restores its position. The force balance seismometers act as a negative feedback (servo) system that causes the mass to follow the motion of the ground. The multiple feedback technique, consisting of different frequency-dependent contributions that shape the closed-loop response of the system, has been adapted to developments of some high-performance seismic sensors capable of detecting seismic signals at a low-noise model as given by Peterson (1993) or better from 0.01 to 30 Hz (Usher *et al.*, 1978, 1979; Wielandt and Streckeisen, 1982).

The presented horizontal component sensor is based on an inverted vertical pendulum, which senses horizontal ground motion. A flat metallic strip of nonferrous alloy in the form of an extended elastic element is used as the suspension mechanism of the proof mass. This elastic element acts as a hinge that exerts the required restoring force to return the mass to its quiescent position. The realization, although simple, clearly approaches the critical issues of the inverted pendulum, such as the pointy axis of rotation, the symmetry of the moving assembly of the pendulum to the perpendicular axis of symmetry, and the long resonant

period. Following the application of frequency-dependent feedback, through a planar electromagnetic actuator, the modified behavior of the sensor exhibits a band-pass response with low- and high-frequency corners at 0.01 and 42 Hz, respectively. The flat part of the transfer function indicates a 750 V/m/sec top velocity.

Mechanical Description of the Sensor

Figure 1 illustrates the general configuration and scaled dimensions of the sensor. The pivot arrangement includes two bearing members. The first is formed around the two clamps (A) that keep the torsion spring, made from chrysocal ($CuSn_3Zn_9$) alloy, in tension like a flat chord; it is coupled with the base plate of the instrument. The second is the mass beam, which is directly fixed on the torsion flat spring (B) by the means of a clamp (C), and extends perpendicularly from the base holding the mass (F) close to its upper end. The elastic element (B) not only pivotally supports the arm (D) on the base of the instrument, but it also forces the arm toward a neutral position. The center of rotation is approximately in the middle of spring width. Thus, the base is moved in the direction of the horizontal plane (shown by arrow K), whereas the seismic mass tends to remain stationary and causes the arm to pivot with respect to the base.

Experiments with various thicknesses and widths of the elastic element have shown that natural periods of several seconds (up to 4 sec) can be achieved with the given mass (0.22 kg) and beam length (0.095 m). In the present case, a 3-sec period was the standard adjustment for the entire study of the instrument and it was achieved by balancing the sensitivity to tilt, the stability of the pendulum motion (null position recovery), and the free period of oscillation, thus facilitating in this manner the initial setup of the sensor.

The following equation (1) describes the motion of an inverted pendulum considering that the mass supporting leg has mass m and moment inertia I_m.

$$(I_m + Ml^2)\ddot{\vartheta} = -k_3 l^2 \vartheta + Mgl\vartheta + mgd\vartheta, \quad (1)$$

where M is the pendulum mass, ϑ is the angle between the vertical axis and the position of mass center, l is the length of the leg, k_3 is the spring constant, I_m is the leg moment inertia, m is the leg mass, d is the distance between the axis of rotation and the center of leg mass, and g is the acceleration of gravity. The angular resonant frequency ω_0 of the inverted pendulum can be derived from equation (2) taking into consideration the previous equation and the fact that the moment inertia of the mass is Ml^2.

$$\omega_0^2 = \frac{k_3 l^2 - (Ml + md)g}{I_m + Ml^2}. \quad (2)$$

Several confounding factors, such as tilting sensitivity, minimum stress of the spring, thermal behavior, the linearity of motion, and null-position recoverability have been examined regarding their influence on the stability and the functionality of the designed sensor. According to the preceding considerations the mass was concentrated bilaterally and perfectly balanced to the perpendicular axis of the symmetry of the supporting beam. Thus, the theoretically estimated cross-talk effect produced by the vertical ground motions when the mass is already excited by horizontal motion is negligible.

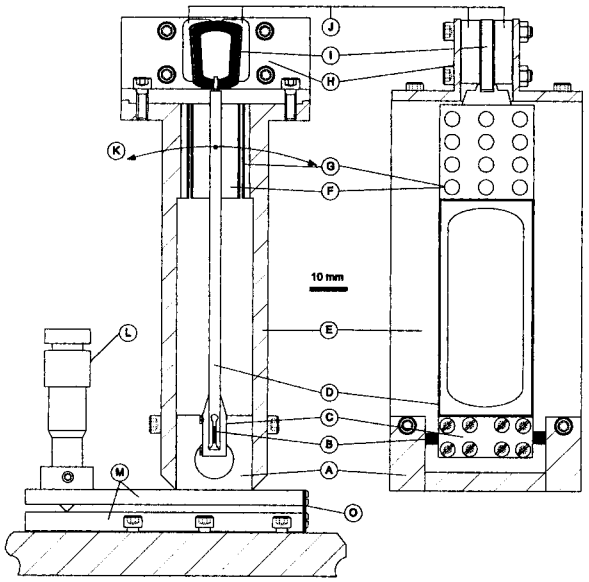

Figure 1. Schematic drawing of side view (left) and front view (right) of the developed inverted pendulum. Capital letters denote as follows: A, clamps that keep the torsion spring in tension; B, torsion spring; C, spring clamp at the bottom end of the pendulum arm; D, pendulum arm; E, rigid lateral members; F, mass; G, capacitance bridge fixed plates; H, magnet block supporting members; I, actuator coil; J, magnet block; K, arrow indicates the direction of pendulum rotation; L, level adjuster; M, base plates

The cantilever beam supports the mass and serves the feedback position and the sensing fine wiring of the sensor. On the upper part of the cantilever beam the mass block is hosted in a place that acts together with the fixed plates (G) as a differential capacitance bridge. The upper end of the beam is completed with the planar feedback coil (I) and the analogous magnet block (H) is fixed on the rigid lateral members (E) of the sensor. The feedback coil is a near-trapezoidal-shaped planar coil, consisting of 340 turns of 0.18-mm magnet wire, with a resistance of 17 Ohms. The magnet assembly consists of two parallel blocks of two NdFeB ($20 \times 10 \times 5$ mm) magnets, respectively (H). The two magnets are laid side-by-side with opposite polarities and are fixed on the ferromagnetic supportive member (H). To approximate the curvilinear type of the pendulum's motion, a wedge-shaped separator between the two magnets corrects the formation of the magnetic flux and optimizes the linearity of the actuator. The 2-mm-thick coil body

moves in the formatted magnet gap with an equilateral clearance of 0.25 mm and exhibits a motor constant of 20 N/A. The sensor is fixed on a heavy stainless steel base plate, equipped with three adjustable legs for leveling. A cylindrical housing protects the sensor against electrostatic charges and isolates the inside of the sensor from the outside environment. Finally, the leveling of the sensor with respect to the ground plane is made by adjusting the vernier (L), which practically affects the parallel setting between the two supportive plates (M). This adjustment could be done either externally by accessing the head of the micromanipulator with a screwdriver or by the possible use of a micro motor and a suitable gearbox inside the sensor housing. The brass spikes used as adjustable legs of the instrument housing have been previously fine beveled for better coupling with the respected brass sockets, and the bolts were replaced with others of finer pitch. A photograph of the developed sensor is shown in Figure 2, with the housing on the left and the internal structure on the right.

Functional Description of the Sensor

A simplified functional diagram of the studied feedback-controlled sensor is shown in Figure 3. Electrical signals that correspond to the kinetic changes of the mass M are amplified and fed back through the electromagnetic actuator to the mass via a multiple-frequency-dependent path, thus closing the servo loop. The output signal V, prior to the application of feedback, could be expressed by equation (3).

$$V(t) = k_2 l p(t), \tag{3}$$

where, k_2 is the displacement constant of the transducer and includes the applied amplification, l is the length between the pivot point and the geometric middle point of the capacitance bridge, and $p(t)$ is the deflection from the null position. To model sufficiently the instrument response over a wide frequency band, it is necessary to estimate not only the servo-sensor dynamics, but also the behavior of the housing-supporting legs. Equation (4) gives the instrument transfer function, including both the ground-to-housing and housing-to-mass motion responses.

$$\frac{V(s)}{X_g(s)} = \frac{X_c(s)}{X_g(s)} \cdot \frac{V(s)}{X_c(s)} \tag{4}$$

where $X_g(s)$ and $X_c(s)$ are the ground and housing motion, respectively, and $V(s)$ the output signal from the servo electronics. Equation (5) can be derived after consideration of the network circuit that affects the coil current (feedback current).

$$i(t) = C\frac{dV}{dt} + \frac{V}{R_1} + \frac{1}{R_2\tau}\int V dt \tag{5}$$

Three different contributions form the current $i(t)$: (1) the proportional current through the resistor R_1, which practically damps the low-frequency oscillation of the system occurring at the lower-frequency corner of the closed loop (at this frequency, the differential and integral feedback fail to maintain the equilibrium of the system, because they have opposite phase and cancel each other); (2) the differential current through the capacitor C (the voltage across the capacitor is proportional to ground velocity); and (3) the in-

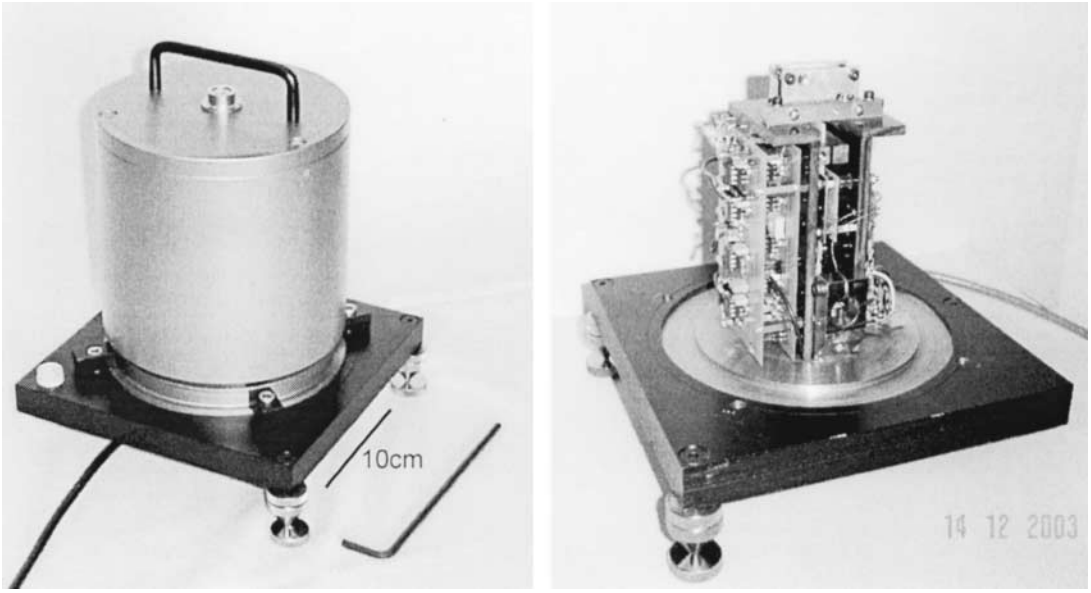

Figure 2. A photograph of the internal structure of the experimental sensor uncovered (right) and covered (left).

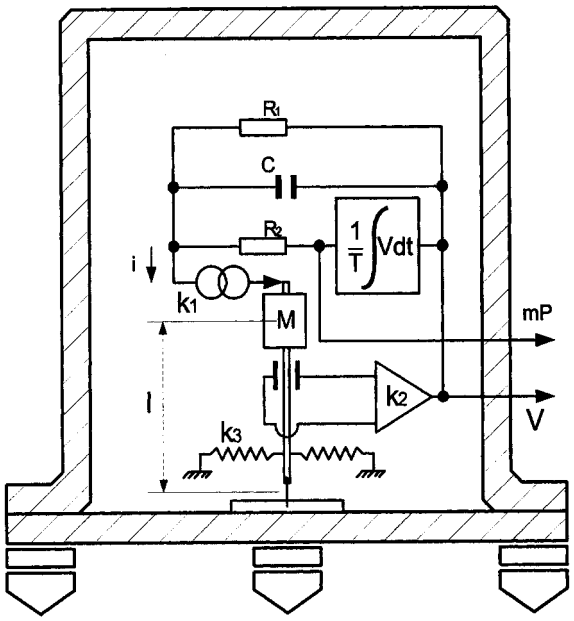

Figure 3. Functional diagram that illustrates the closed loop of the experimental sensor. An error signal, associated with the position of the intertial mass against the frame of the instrument, is amplified by k_2 and fed to the feedback actuator k_1. The total current i is the sum of three different currents passed through R_1, C, and R_2, which is the integrator's output. M is the seismic mass, l is the length of the leg, k_3 is the spring constant representing the stiffness of the pivot element, V is the velocity broadband output, and mP the mass position output signal.

tegral current through the resistor R_2, which is derived from the integration of the output voltage with a time constant τ (this current suppresses the long period disturbances of the mass).

The expression (6) describes the output voltage given the mass displacement constant k_2. The relation of the feedback current could be derived by equation (7) given the motor constant k_1, the mass M, and the acceleration $\ddot{x}_m$.

$$V(t) = k_2 x_m \tag{6}$$

$$k_1 i = -M\ddot{x}_m. \tag{7}$$

Expressions (8) and (9) form the transfer function of the system regarding the output $V(s)$ and the housing $X_c(s)$ motion.

$$\left[Cs + \frac{1}{R_1} + \frac{1}{R_2\,\tau s}\right]V(s) = -\frac{Ms^2}{k_1}\left[\frac{1}{k_2}\,V(s) + X_c(s)\right]. \tag{8}$$

$$\frac{V(s)}{X_c(s)} = \frac{\dfrac{-Ms^2}{k_1 C}}{\dfrac{M}{k_1 k_2 C}\,s^3 + s^2 + \dfrac{1}{R_1 C}\,s + \dfrac{1}{R_2 C\tau}}. \tag{9}$$

$$h = (2R_1)^{-1}\,(\tau R_2/C)^{1/2}. \tag{10}$$

As shown in (9), the parameters that could modify the closed-loop behavior of the system are components that shape the total feedback current as a function of frequency. In the previously mentioned expression the part of the function that describes the behavior of the base legs is omitted for reasons of simplicity. Figure 4 illustrates the theoretical response curve of the experimental seismometer given the values of $M = 0.22$ kg, $k_1 = 20$ N/A, $k_2 = 200{,}000$ V/m, $R_1 = 800$ kΩ, $R_2 = 240$ kΩ, $C = 15$ μF, and $\tau = 80$sec. By using this set of values the flat part of the response curve corresponds to 750 V/m/sec with damping constant $h = 0.7$ as it is derived from expression (10). As shown in Figure 4, the -3 dB line that corresponds to the flat part crosses the response curve at 0.01 and 42 Hz, respectively.

Standard techniques were used for the amplification and synchronous demodulation of the differential capacitance bridge signal with special emphasis for the low-noise properties of the used active components of the circuit. The acquisition and measurement requirements, during the development of the sensor and testing period, were supported by a Keithley digitizer and Testpoint (Capital Equipment) software package, whereas the recordings, during the evaluation period, were made at the ATH seismic station of the Institute of Geodynamics, National Observatory of Athens, through a six-channel DR-24 (Geotech Instruments) 24-bit digitizer

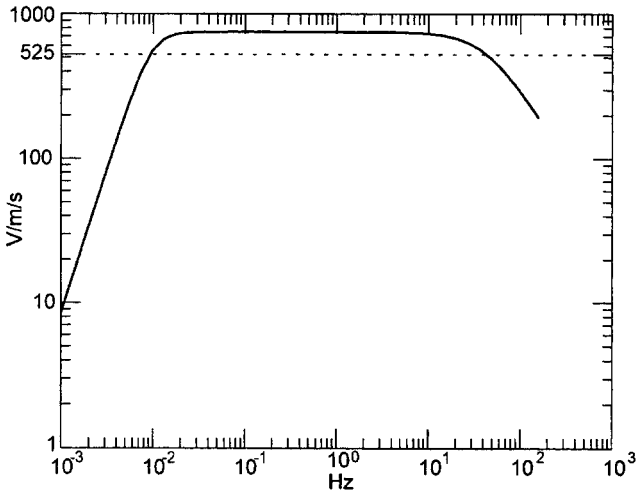

Figure 4. The plot illustrates the theoretical response curve of the experimental seismometer defined by its transfer function. The response is expressed in volts per meter per second as a function of frequency. The -3 dB level line crosses the response curve at 0.01 and 42 Hz, respectively.

in combination with standard reference instrumentation at ATH vault (i.e., Streckeisen STS-2 and Guralp CMG40T seismometers). All the north–south components used during the evaluation period were recorded by the same digitizer (DR-24). Hence, the observed differences, during comparative analyses, in the recorded signals referred only to the sensor responses. MATLAB v6.5 was used as the standard mathematical tool for the study of the sensor dynamics and performance.

Sensor Self-Noise

The Brownian motion of the air molecules inside the sensor capsule is a considerable noise source especially in light-mass pendula. The way this type of motion affects the proof mass has been described in Aki and Richards (1980; see volume 1, section 10.3.1). A comparative study by Riedesel *et al.* (1990) has shown that the sensitivity of light-mass and short-period inertial sensors is limited because of this type of noise. The power spectral density (PSD) of the acceleration caused by the Brownian motion can be derived from:

$$a = \frac{8\pi kT}{MPQ}, \tag{11}$$

where, α is the acceleration power spectral density, $k = 1.38 \times 10^{-23}$ J/°K the Boltzmann's constant, T is the absolute temperature, M is the mass, P is the period, and Q is the quality factor of the sensor, which describes the energy loss in each cycle of oscillation due to dissipation and characterizes the quality of the suspension and the friction between the moving part of the pendulum and the air. In the present case the estimated Brownian motion noise was found 4×10^{-20} $(\mathrm{m/sec^2})^2$/Hz expressed in acceleration power spectra density and has the form of a constant function in the frequency domain. This value is below the distribution that defines the new global low-noise model (LNM), in acceleration units, as given by Peterson (1993). Equation (11) simply describes the theoretical thermal noise level of a suspended mass in a standard atmosphere, where the motion is limited by a dissipative damping system. In practice several permanent or transient mechanical stresses on the spring and the suspension mechanism could produce higher levels of mechanical noise than the Brownian. In these cases, effects such as the microbending, creep, and structural deformation of the spring or the hinge element contribute toward systematic errors and nonlinearities in measuring displacements even in the nanometer range. In the present case, during the long-term monitoring period, transient (i.e., spikes) or systematic noises (i.e., creep of the flexure) related to the structure of the flexure were not observed.

In general, the long-period noise caused by the internal convection current due to the dissipation of the circuits must be taken into consideration. In the present case, the specific mass position in relation to the up-going stream of air molecules is theoretically expected to result toward low-level, long-period noise. In addition, this parameter could be more significant in vertical component designs, where the suspended mass is exposed to the vertical convection draft. To overcome this effect, the circuit boards have to be either thermally isolated from the sensor compartment or the air must be evacuated.

Comparisons of Ground Noise Power Spectral Estimations

The total noise distribution of the experimental seismometer, which is the sum of the instrumental, ground, and environmental noise, was estimated by a simple comparison against the noise PSD records obtained from Streckeisen STS-2 placed at the same vault (in our case the ATH seismic station), which can be considered as a highly sensitive reference instrument. Average noise velocity PSD estimates between 100 and 0.1 sec were calculated for the north–south components of the Streckeisen STS-2, Guralp CMG40T (30 sec), and the experimental seismometers, respectively, by adopting a data selection procedure such as followed by Wilson *et al.* (2002). Thus, preliminary determination of epicenters reported by the Institute of Geodynamics, National Observatory of Athens, and the European Mediterranean Seismological Center were referred to in selecting data windows to avoid earthquake signals according to the following criteria: (1) no earthquakes with $m_b \geq 6.0$ reported in the preceding 24 hr; (2) no earthquakes with $m_b \geq 5.0$ reported with $\Delta \leq 70°$ in the preceding 24 hr; (3) no earthquakes with $m_b \geq 4.0$ reported for $\Delta \leq 20°$ in the previous 12 hr; (4) no earthquakes with $m_b \geq 3.0$ reported for $\Delta \leq 15°$ in the previous 3 hr. The specific noise figure for the ATH seismographic station corresponds to a relatively quiet day (23 to 25 July 2004) in terms of cultural noise and weather conditions during the after midnight (UTC) hours.

Figure 5 shows the noise spectra of STS-2, CMG40T (30 sec), and experimental seismometers at the ATH vault. Each PSD is the average of five computations obtained from five, 75% overlapped, velocity signal epochs with lengths of 45,000 data points each sampled at 50 Hz (900-sec time window). In the same figure are plotted together the LNM plot and the new high-noise model (HNM) curves obtained by Peterson (1993). There is a peak value in the area of 7–8 sec that indicates the microseismic activity at ATH station and it has the same pattern for all the sensors compared in the present test. For the period ranging from 10 to 100 sec the slopes of STS-2 and experimental PSDs are close together exhibiting morphological similarities. A possible interpretation for the differences found in the this period range between the two instruments could be the effect of the temperature changes during the recording period, which differently influenced the suspension of the two instruments. Also, tilt from wind and pressure variations can be, and usually is, different in different places on the same pier. Tilt noise is a

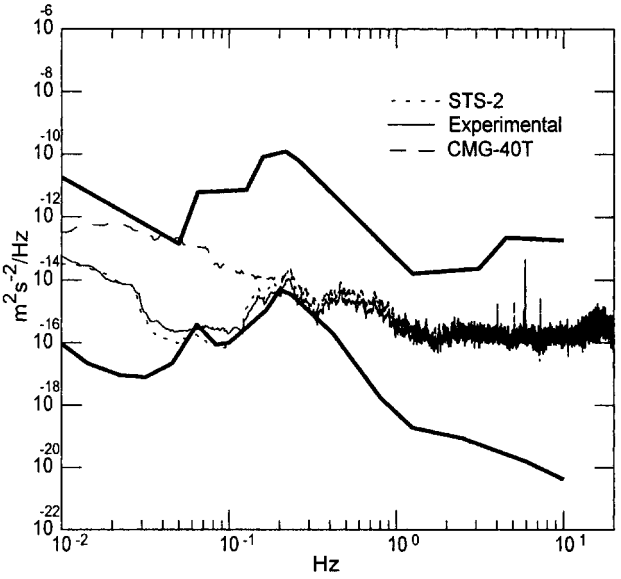

Figure 5. Distribution of noise power spectral densities at ATH seismic station. Each PSD is the average of five computations obtained from five, 75% overlapped velocity signal epochs of 45,000 data points each sampled at 50 Hz. Solid, dashed, and dotted lines represent the experimental, CMG-40T, and STS-2 seismometers, respectively.

common problem with horizontal seismometers, especially in the long period (LP) band.

Comparisons of Teleseismic and Regional Recordings

To evaluate the resolution and the behavior of the experimental seismometer, several teleseismic and regional events were analyzed during the side-by-side recording period on the ATH vault. Three representative examples, two teleseismic and one regional, were chosen to serve the purpose of the present study.

Figure 6 presents velocity records at ATH vault of the Fiji earthquake (Origin time, 15 July 2004 04:27:05.4; M_w 7.0; location, 17.22S 178.89W; depth, 500 km), recorded by STS-2 and the experimental seismometer. The plotted velocity amplitude signals are down-sampled 1-Hz seismograms for the main (Fig. 6a) and the zoomed detail window (Fig. 6b), respectively. Amplitude and phase can be seen as approximately coincided for both sensors with the experimental to follow the wave configuration pattern of the STS-2 (Fig. 6b). The spectral analysis of the selected window (Fig. 6c) indicates similarities in the spectral shape within the range of 0.5 to 0.05 Hz for both instruments, whereas the differences found in the range of 0.05 to 0.01 Hz are in accordance with the different low-frequency corner of STS-2 (120 sec) and experimental (100 sec), respectively.

Figure 7 presents velocity records at ATH vault of the Southern Sumatra, Indonesia earthquake (Origin time, 25 July 2004 14:35:17.6; M_w 7.1; location, 2.35S 104.04E; depth, 575 km], recorded by STS-2, Guralp CMG40T (30 sec), and the experimental seismometer. In a similar manner to Figure 6, in this example Figure7a shows the main selected window and Figure 7b, c shows the zoomed detail window and spectra, respectively. The similarities on the velocity amplitude and spectral data are the same as the previous example shown in Figure 6. In addition, Figure 7d shows the estimated magnitude squared coherence function between STS-2 and the two experimental and Guralp CMG40T(30sec) seismometers, indicating the rate of similarity as a function of frequency.

Figure 8 presents velocity records at ATH vault of the Aegean Sea earthquake (Origin time, 25 July 2004 22:35:41.5; M_L 3.8; location, 39.59N 23.70E; depth, 13 km), recorded by STS-2, Guralp CMG40T (30 sec), and the experimental seismometer. In a manner similar to Figure 6, in this example Figure 8a shows the main selected window and Figure 8b, c shows the zoomed detail window and spectra, respectively. For this regional event the sampling rate for both plot and analysis purposes was 50 Hz. The three velocity signals (Fig. 8b) are morphologically identical, and in the frequency domain (Fig. 8c) the respected spectral lines practically overlap each other.

Discussion

In the present study, an inverted vertical pendulum design was applied. This, in the absence of feedback control, behaves as a mechanical harmonic oscillator that makes it possible to obtain low-resonant frequency in the horizontal direction. The low-resonant frequency cannot be ignored in the design of feedback broadband sensors, because it constitutes a significant parameter, if low-frequency and low-amplitude displacement are targeted (Wielandt, 2004).

The flat spring made from chrysocal ($CuSn_3Zn_9$) alloy used as pivot-suspension assembly exhibited better thermal performance than materials based on stainless steel, which were tried initially. Although the conventional cross-spring assemblies exhibit characteristics similar to the previously mentioned assembly, they are considered as fixed-pivot elements that limit the experimentations in regard to the torsional spring rate and load capacity parameters, which were essential in the design of the proposed pendulum.

The force-balanced principle exploits a well-known measurement method that is also used in many other disciplines related, in general, to mass motion. Following this principle, a secondary derived quantity that is required to keep the system in a steady state is measured instead of the quantity that directly excites the system. One of the advantages that this technique introduces is that the seismic mass remains steady. This means (at least in a first-order approximation) that all nonlinearities of the suspension spring are irrelevant and the spring should theoretically never be stressed and strained. The amplitude resolution only still depends on the mechanical part.

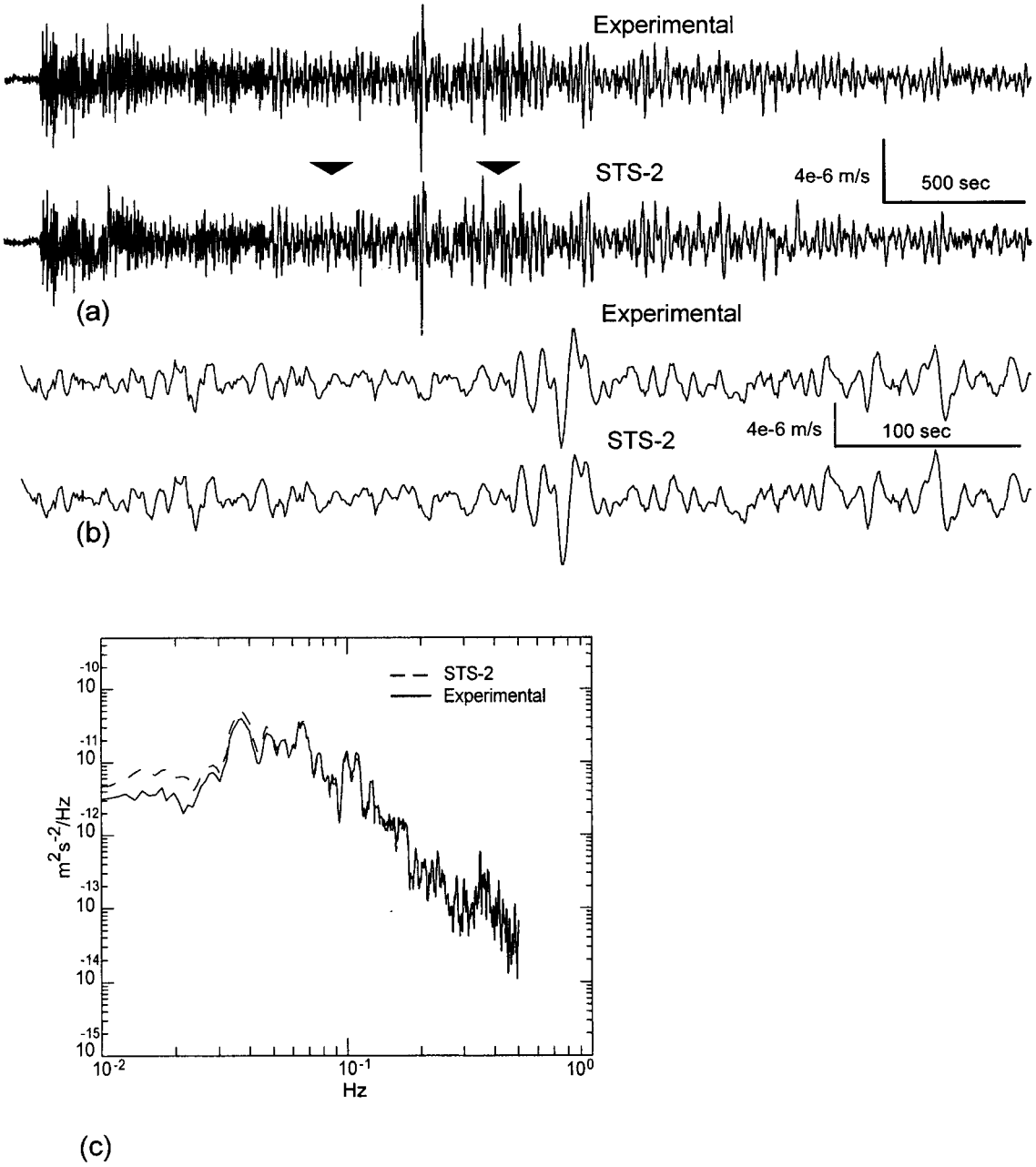

Figure 6. The Fiji Islands earthquake as recorded at the ATH vault (Origin time, 15 July 2004 04:27:05.4; M_W 7.0; location, 17.22S 178.89W; depth, 500 km). (a) Velocigrams sampled at 1 Hz. The two triangular marks indicate the zoomed window shown in (b). (c) The corresponding velocity power spectral densities of the zoomed window. Solid and dashed lines indicate the experimental and STS-2 window densities, respectively.

According to this principle, short-period designs have been electronically tuned to behave theoretically as broadband, allowing even less sophisticated designs of the suspension mechanism to perform sufficiently well at low frequencies. However, in the present development, parameters such as the pendulum natural period, mass, and Q factor of the suspension were considered following the criticism that has been noted in the literature (Wielandt, 2004; Teupser and Plesinger, 1979).

The signal obtained from the differential capacitance displacement bridge has been treated by lock-in amplifier circuitry. Although, this technique can recover in principal the signal from +100 dB (max) internal broadband noise, some noise sources still remain in the feedback loop. The integrator that functions in the integral path of the feedback loop is realized with two at least operational amplifiers. This circuitry contributes to the generation of low-frequency noise, which is caused by the semiconductors and the non-

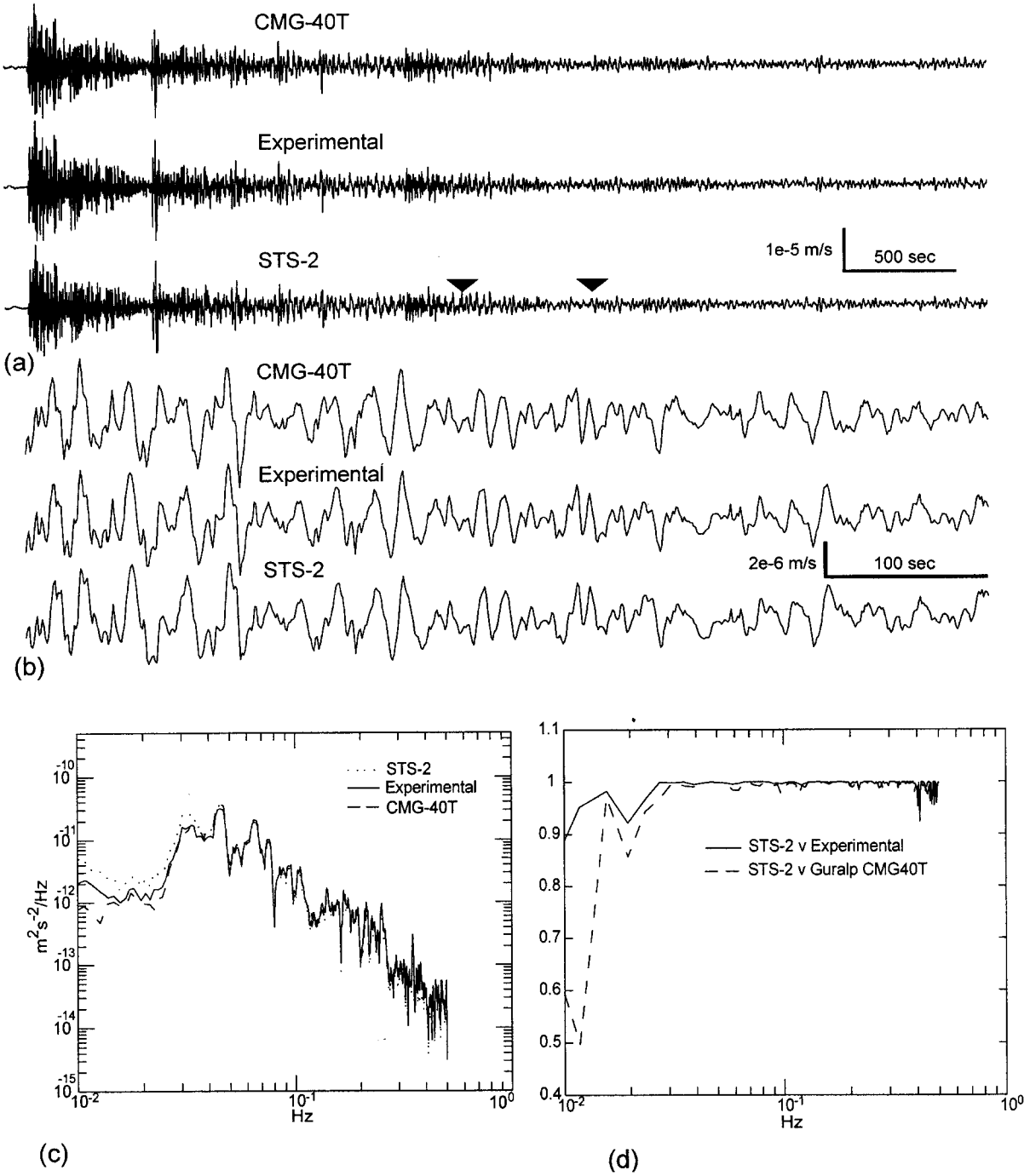

Figure 7. The Sumatra, Indonesia earthquake as recorded at the ATH vault (Origin time, 25 July 2004 14:35:17.6; M_W 7.1; location, 2.35S 104.04E; depth, 575 km). (a) Velocigrams sampled at 1 Hz. The two triangular marks indicate the zoomed window shown in (b). (c) The corresponding velocity power spectral densities of the zoomed window. Dashed, solid, and dotted lines indicate the CMG-40T, experimental, and STS-2 window densities, respectively. (d) Corresponding cross-spectral densities. Solid and dashed lines are the cross-spectral densities between STS-2 versus experimental and STS-2 versus CMG-40T seismometers, respectively. The signals are downsampled at 1 Hz.

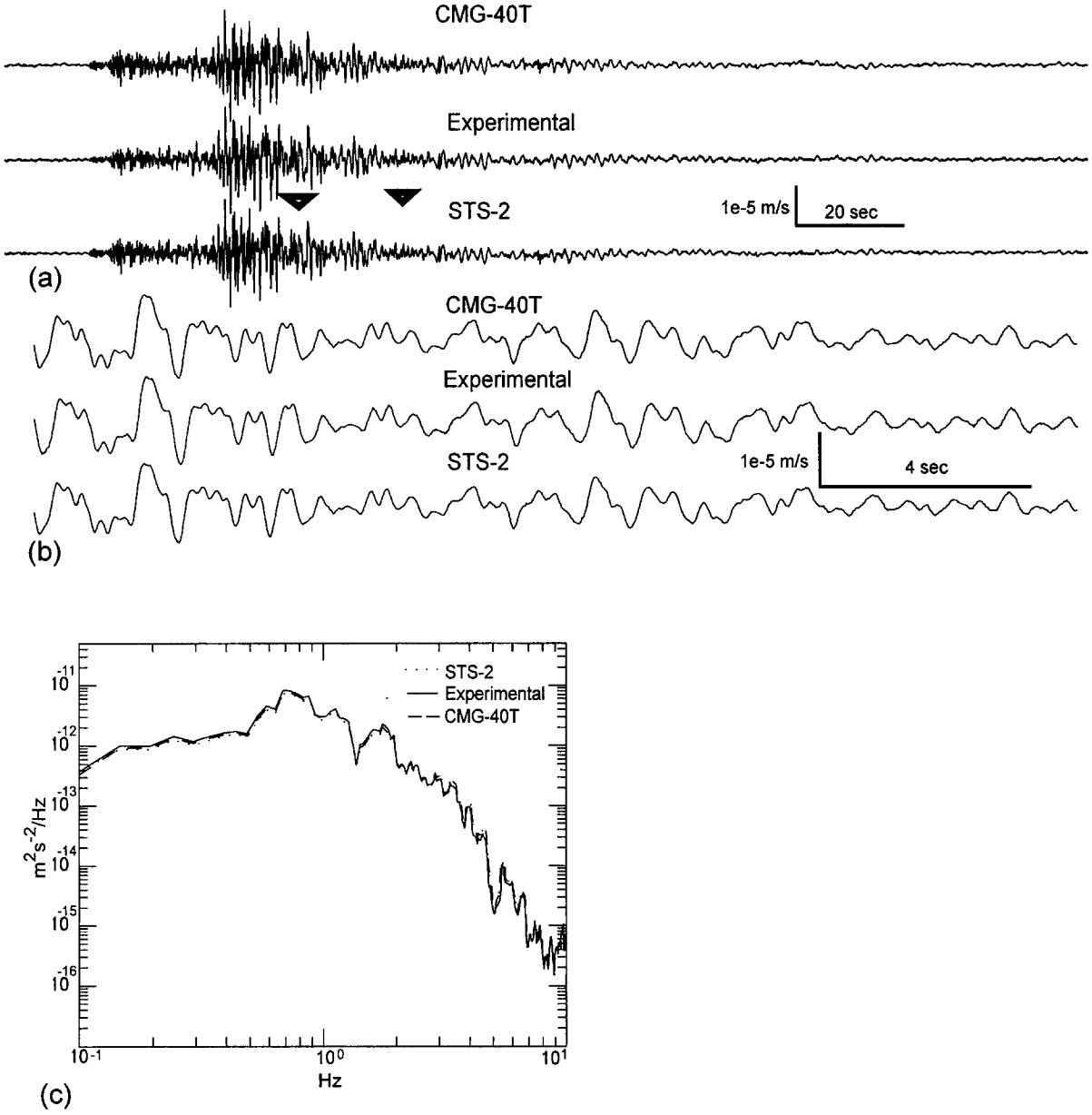

Figure 8. The Aegean Sea earthquake as recorded at the ATH vault (Origin time, 25 July 2004 22:35:41.5; M_L 3.8; location, 39.59N 23.70E; depth, 13 km). (a) Velocigrams sampled at 50 Hz. The two triangular marks indicate the zoomed window shown in (b). (c) Corresponding velocity power spectral densities of the zoomed window. Dashed, solid, and dotted lines indicate the CMG-40T, experimental, and STS-2 window densities, respectively.

ideal behavior or instabilities of the passive components used for the completion of the integrator. In the present development, to reduce this specific type of noise, a less strong integral-path feedback was selected. The finally selected value of R_2 resulted from various computations of the sensor transfer function, taking into consideration the interaction between the dominant capacitance feedback current and the integral current.

The preceding selection imposed that the acceptable boundaries of the mass position due to the initial and or long-term tilting and temperature influences are narrowed, in comparison with the strong integral-feedback selection that needs no initial or periodical mass centering.

Tests with inclination experimentations showed that effective mass-position recovery can be achieved between $\pm 2°$. In practice, after the initial leveling of the sensor using the water bubble level and the adjustable legs, a more precise and slow enough leveling procedure can take place with adjustment of the vernier (L) and observation of the mass position output signal (denoted as mP on Fig. 3) output voltage.

The planar coil-magnet actuator, used for the feedback interaction with the suspended mass, offered linear motion of the coil inside the uniform magnetic field, without the restrictions seen in the tubular-formed voice coil actuators due to the axial movement of the coil. The strong magnetic field inside the NdFeB magnet block increased the motor constant of the assembly. This critical parameter could potentially be increased further by decreasing the gap between coil and magnet with a finer mechanical approach in the construction of the actuator.

The work presented mainly focused on the properties of the specific inverted pendulum design that uses the same element as both suspension and spring. The center of pendulum rotation is defined at one point, instead of the distributed rotation along a flexible beam, when such type of suspension is used to hold and maintain the seismic mass inverted. Several local, regional, and teleseismic earthquakes recorded at the ATH vault were selected for investigation and comparison with Streckeisen STS-2 (120 sec) and Guralp CMG40T (30 sec) sensors placed side by side with the developed experimental seismometer. Recorded waveforms were analyzed and their comparison showed to be compatible in terms of amplitude and frequency response indicating the capability of the experimental sensor to resolve low frequency and amplitude seismic signals.

Acknowledgments

We thank Prof. C. Stefanis, Director of the Athens University Mental Health Research Institute, for his support and encouragement toward a well-established Laboratory for the Processing of Electrophysiological signals that made possible the present development. Thanks also to Dr. G. Stavrakakis, Director of the Institute of Geodynamics, National Observatory of Athens, for his discussions and comments. Dr. G. Drakatos is thanked for introducing the two authors, which made possible the present work. Last but not least we thank Dr. A. Michael, the Editor in Chief, Dr. Bob Hutt, and an anonymous reviewer for their fruitful criticism in improving the initial manuscript.

References

Aki, K., and P. G. Richards (1980). *Quantitative Seismology: Theory and Methods*, Vol. 1, W. H. Freeman and Company, San Francisco, 572 pp.

Daniel, R. G. (1979). An intermediate-period field system using a short-period seismometer, *Bull. Seism. Soc. Am.* **69,** 1623–1626.

Melton, B. S. (1979). The sensitivity and dynamic range of inertial seismographs, *Phys. Earth Planet. Interiors* **18,** 64–70.

Muramatsu, I., T. Sasatani, and I. Yokoi (2001). Velocity-type strong motion seismometer using a coupled pendulum: design and performance, *Bull. Seism. Soc. Am.* **91,** 604–616.

Peterson, J. (1993). Observations and modeling of seismic background noise, *U.S. Geol. Surv. Open-File Rept. 93-322.*

Riedesel, M. A., R. D. Moore, and J. Orcutt (1990). Limits of sensitivity of inertial seismometers with velocity transducers and electronic amplifiers, *Bull. Seism. Soc. Am.* **80,** 1725–1752.

Roberts, P. M. (1989). A versatile equalization circuit for increasing seismometer velocity response below the natural frequency, *Bull. Seism. Soc. Am.* **79,** 1607–1617.

Teupser, C., and A. Plesinger (1979). Design of feedback-controlled wide-band seismographs with respect to undesired side-effects, *Phys. Earth Planet. Interiors* **18,** 58–63.

Usher, M. J., R. F. Burch, and C. Guralp (1979). Wide-band feedback seismometers, *Phys. Earth Planet. Interiors* **18,** 38–50.

Usher, M. J., C. Guralp, and R. F. Burch (1978). The design of miniature wideband seismometers, *Geophys. J. R. Astr. Soc.* **55,** 605–613.

Wielandt, E. (2004). Design considerations of broadband seismometers, Presented at *IRIS Advanced Broadband Seismometer Workshop*, 24–26 March 2004, Lake Tahoe, California.

Wielandt, E., and G. Streckeisen (1982). The leaf-spring spring seismometer: design and performance, *Bull. Seism. Soc. Am.* **72,** 2349–2367.

Willmore, P. L. (1979). Developments in electromagnetic and hybrid seismometers, *Phys. Earth Planet. Interiors* **18,** 35–37.

Wilson, D., J. Leon, R. Aster, J. Ni, J. Schue, S. Grand, S. Semken, S. Baldridge, and W. Gao (2002). Broadband seismic background noise at temporary seismic stations observed on a regional scale in the Southwestern United States, *Bull. Seism. Soc. Am.* **92,** 3335–3341.

Signal Processing Laboratory
University Mental Health Research Institute
P.O. Box 66517
GR-156 01 Papagou
Athens, Greece
elkoutsl@otenet.gr
(E.K.)

Institute of Geodynamics
National Observatory of Athens
Lofos Nimfon, Thisio
GR-118 10 Athens, Greece
nmelis@gein.noa.gr
(N.S.M.)

Manuscript received 10 March 2005.